CHEMISTRY OF MATERIALS

pubs.acs.org/cm

Article

Rotator Phases in Chemically Recyclable Oligocyclobutanes

Hang Zhang, Shawn M. Maguire, Cherish Nie, Rodney D. Priestley, Paul J. Chirik, Richard A. Register, Emily C. Davidson, and Michael A. Webb*

Cite This: *Chem. Mater.* 2024, 36, 11596−11605

Read Online

ACCESS | Metrics & More | Article Recommendations | Supporting Information

ABSTRACT: Rotator phases are rotationally disordered yet crystalline stable states found in many materials. The presence of a rotator phase leads to unique properties that influence processing methods and offer potential applications in areas such as thermal energy storage, lubrication, and sensing. Recently, a novel family of chemically recyclable oligomers, (1,*n*′-divinyl)-oligocyclobutane (DVOCB(*n*)), has shown evidence of rotator phases. This study combines experimental characterization and molecular dynamics simulations to confirm and elucidate the rotator phases in DVOCB(*n*). Compared with well-studied *n*-alkanes, DVOCB(*n*) exhibits distinct structural, thermodynamic, and dynamical characteristics. The crystal-to-rotator phase transition of DVOCB(*n*) involves a shift from stretched to isotropic hexagonal lamellar packing, captured by a rotational order parameter tracking local chain orientations orthogonal to the chain axis. Unlike *n*-alkanes, where rotational relaxation times are constant and long in the crystal phase before dropping dramatically during the crystal-to-rotator phase transition, relaxation times decrease more gradually upon heating in DVOCB(*n*), including continuously throughout the transition. This behavior is attributed to its unique enchained-ring architecture, which allows for semi-independent rotation of chain segments that promotes overall rotational disorder. This work provides a fundamental understanding of rotator phases in DVOCB(*n*) and highlights differences from those of conventional materials. The analyses and insights herein will inform future studies and applications of DVOCB(*n*) as well as other materials with rotator phases.

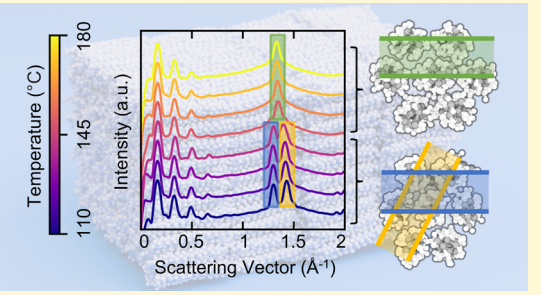

Downloaded via PRINCETON UNIV on April 9, 2025 at 21:33:28 (UTC).
See https://pubs.acs.org/sharingguidelines for options on how to legitimately share published articles.

1. INTRODUCTION

Rotator phases are intriguing stable states that can be found in certain organic and polymeric materials. They feature regular, ordered structures like crystalline phases but also exhibit some rotational freedom.[1−3] This rotational freedom is usually restricted to the longitudinal axis of polymer chains or segments and can impart fluidity to the material. The presence of a rotator phase can substantially influence physical properties. This can manifest in unique melting characteristics and complex viscoelastic responses. Such behaviors have implications for various applications, such as in lubricants,[4] self-shaping droplets,[5] lipid biomembranes,[6] fuels,[7] and phase-change energy-storage materials.[8] Rotator phases and liquid-crystalline phases share similarities,[9,10] such as hexagonal in-plane order seen in both the R_{II} rotator phase of *n*-alkanes and smectic-B phases.[11] In fact, rotator phases could be considered a subset of smectic-B phases but with rotational dynamics and disordering that enhance their plasticity.[9] Whereas smectic-B phases are found in mesogens with rigid core structures,[12,13] rotator phases are typically found in alkanes and oligomers, possibly polydisperse. Therefore, understanding the presence and characteristics of rotator phases is of both fundamental and potential technological interest.

Rotator phases have been reported for several systems.[2,14−18] Due to their simple structure and widespread use, *n*-alkanes have been most extensively studied.[1,5,9,10,19,20] Common experimental techniques for characterizing rotator phases include X-ray scattering, nuclear magnetic resonance, and infrared and Raman spectroscopy.[1,9,19−22] For instance, Sirota et al. identified five distinct rotator phase transitions for *n*-alkanes with 20−33 carbon atoms by analyzing temperature-dependent X-ray scattering profiles.[11,19] Molecular dynamics (MD) simulations have provided complementary molecular-level insights to these experimental characterizations.[23−27] Wentzel and Milner demonstrated that well-crafted force fields could accurately capture phase transitions and temperatures, in agreement with experiments. By identifying useful molecular, structural order parameters, the authors could discriminate among different phases and illustrate weakly first-order transitions.[26,28] Burrows et al. utilized MD simulations to characterize alkane structure at the water interface to provide insights about the influence of rotator phases on the self-shaping of oil droplets in surfactant solutions.[27,29,30] Nevertheless, detailed molecular-level investigations of rotator phases

Received: September 12, 2024
Revised: November 11, 2024
Accepted: November 20, 2024
Published: November 28, 2024

ACS Publications

© 2024 American Chemical Society

in other materials and how they compare to the comparatively well-characterized *n*-alkanes remain limited.

Recent experimental work has indicated the likely presence of crystal-to-rotator phase transitions for a new family of materials based on (1,*n*′-divinyl)oligocyclobutane (DVOCB).[32,33] DVOCB is oligomerized through iron-catalyzed sequential [2 + 2]-cycloaddition of butadiene. This produces an intriguing 1,3-enchained cyclobutyl architecture (Figure 1A,B), denoted as DVOCB(*n*). The four-carbon ring

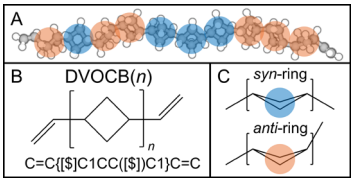

Figure 1. Structural characteristics of a DVOCB(*n*) chain. (A) Molecular rendering of a single DVOCB(10) oligomer. The structure consists of a series of cyclobutyl rings as the oligomer backbone. Cyclobutyl rings exhibit geometrical isomerism based on the ring-carbon stereochemistry. These are referred to as *syn* (blue), for which adjacent rings are on the same side of the labeled ring, and *anti* (orange), for which adjacent rings are on opposing sides of the labeled ring. (B) Skeletal structure and BigSMILES notation[31] for DVOCB-(*n*). The BigSMILES string of DVOCB(*n*) is C═C{[$]C1CC([$])-C1}C═C. (C) Skeletal diagrams distinguishing the connectivity of *syn* (blue) and *anti* (orange) rings.

structure can also present distinct stereochemistries, resulting in geometrical isomerism distinguished as *syn*, if bonding to adjacent rings occurs on the same side of the ring, or *anti*, if bonding to adjacent rings occurs on opposing sides of the ring (Figure 1C). Promisingly, DVOCB(*n*) can be deoligomerized back to pristine butadiene.[32] Furthermore, there are synthetic strategies to polymerize DVOCB(*n*) into chain-extended, chemically recyclable polyolefins with tunable thermomechanical properties; these materials also likely possess rotator phases.[33] Understanding the characteristics of rotator phases for DVOCB(*n*) and derivative materials could have ramifications for processing, controlling crystallization behavior, resulting thermomechanical properties, and (de)-polymerization efficiency.

In this work, we investigate rotator phases in DVOCB(*n*) using a combination of experimental characterization and MD simulation. The MD simulations are facilitated by developing a new force field that addresses the complexities of the 1,3-enchained cyclobutyl architecture. Experimental X-ray scattering measurements and simulations display similar trends in crystal-to-rotator phase transitions during the heating process. MD simulations are then used to provide insight into the structural characteristics and origins of the rotator phase in DVOCB(*n*) systems. This analysis is further informed and contextualized by explicit comparisons to comparable *n*-alkane systems. We find that the ring structure in DVOCB(*n*) imparts functionally distinct rotator phase behavior relative to that of the linear *n*-alkanes. Ultimately, this study specifically elucidates properties for an emerging class of chemically recyclable materials while also more broadly informing on possible manifestations and analyses of rotator phases.

2. METHODS

2.1. Experiment. *2.1.1. Materials.* The DVOCB(*n*) oligomers (*n* = 4, M_n = 270 g/mol, $Đ$ = 1.05; *n* = 5, M_n = 325 g/mol, $Đ$ = 1.05; *n* = 6, M_n = 379 g/mol, $Đ$ = 1.04; *n* = 8, M_n = 487 g/mol; *n* = 10, M_n = 596 g/mol) were prepared according to the procedures described in ref 33. We note that the experimentally prepared DVOCB(*n*) has narrow but not monodisperse distributions, whereas prior studies of *n*-alkanes are practically monodisperse materials. Unless otherwise specified, all reagents and solvents were purchased commercially and used as received without further purification.

2.1.2. Wide-Angle and Small-Angle X-ray Scattering. Wide-angle and small-angle X-ray scattering (WAXS and SAXS) measurements were performed on a Xenocs Xeuss 3.0 in-lab beamline using a Cu–K_α source. In situ measurements with heating were made by using a heating rate of 5 °C/min with a Linkam heating stage and an in-house temperature calibration curve. The details about the temperature calibration are given in Section S1 of the Supporting Information. The distance between the detector and the sample was calibrated using the primary (100) reflection, 2θ = 21.358°, of a lanthanum hexaboride (LaB_6, simple cubic[34]) standard under WAXS high-resolution beam conditions. Oligomer samples for scattering measurements were prepared as follows. A dried oligomer powder was loaded into a steel washer of dimensions of ca. 0.5 mm thick and 5.0 mm inner diameter. Using a melt press, the samples were heated above their melting temperature and compressed to form a disk-shaped specimen; the washer was sandwiched between Kapton sheets to limit thermally induced oxidation during processing. The oligomer disk was then punched out of the washer using a steel rod and loaded into Linkam heating cells, ensuring good thermal contact. Prior to data collection, samples were heat cycled to above their melting temperature and then cooled at 5 °C/min to match the DSC cooling conditions and eliminate any processing effects on crystallinity. Finally, raw two-dimensional scattering images were collected on heating for 10 min per sample under high-resolution beam conditions and then azimuthally integrated into one-dimensional patterns for further analysis.

2.1.3. Differential Scanning Calorimetry. All DSC samples were run using a TA Instruments DSC 2500, and data analysis was performed with TA Instruments TRIOS software. Polymer samples for differential scanning calorimetry (DSC) were prepared as follows. Between 3 and 10 mg of material was loaded into aluminum Tzero Pans; powders were gently tamped down using a steel rod to generate a uniform powder layer and good thermal contact with the bottom of the pan. The pan was then crimp-sealed with an aluminum lid. Samples were ensured to run under inert conditions by making a pinhole in the center of the top side of the crimped DSC sample. For all DSC traces, two heating–cooling cycles were performed at a heating–cooling rate of 5 °C/min. The value of each thermal transition was obtained from the second heating to mitigate the effects of thermal history. More details about DSC are given in Section S2 of the Supporting Information.

2.2. Simulation. *2.2.1. General Simulation Procedures.* All simulations used version 3 Mar 2020 of the LAMMPS simulation package.[35] Periodic boundary conditions were used in all dimensions. The equations of motion were evolved using a velocity Verlet integration scheme and a 1 fs time step. Real-space nonbonded interactions were truncated at 14 Å for all simulations. For DVOCB(*n*) systems, the long-range electrostatics were handled with PPPM[36] with 0.00001 convergence accuracy. Isothermal–isobaric simulations were performed with a Nosé–Hoover thermostat and barostat[37] with damping constants of 100 and 1000 fs, respectively. Interactions for DVOCB(*n*) systems were described with a force field based on an adaptation (see Section 2.2.2) of the topology automated force-field interactions (TAFFI) framework.[38] Interactions for *n*-alkane systems were described using the Flexible Williams 4 (FW4) force field.[39] The FW4 force field was chosen because it was previously found to capture characteristics of crystal-to-rotator phase transitions in good agreement with experiments.[26−28] Simulation cells were prepared for DVOCB(*n*) with *n* = 5, 7, and 10 and for *n*-alkane, C_nH_{2n+2}, with *n* = 23, 27, and 31. These systems were chosen such that the DVOCB(*n*) systems would have end-to-end lengths comparable to those of *n*-alkanes with notable evidence of crystal-to-rotator phase transitions. Production simulations were

https://doi.org/10.1021/acs.chemmater.4c02576
Chem. Mater. 2024, 36, 11596−11605

performed at a series of temperatures that spanned observation of both crystal and rotator phases to obtain data for analysis. For DVOCB(5), DVOCB(7), and DVOCB(10), the temperature ranges were [−5, 90 °C], [55, 150 °C], and [105, 210 °C] with simulations performed at 5 °C intervals. For $C_{23}H_{48}$, $C_{27}H_{56}$, and $C_{31}H_{64}$, the temperature ranges were [10, 100 °C], [20, 110 °C], and [40, 130 °C] with simulations performed at 10 °C intervals. More details about system preparation and production are given in Section S4 of the Supporting Information.

2.2.2. Parametrization of DVOCB(n) Systems. During preliminary work, we found that existing classical force fields (e.g., all-atom optimized potentials for liquid simulations, OPLS-AA[40]) did not adequately describe conformational characteristics of the enchained rings present in DVOCB(n). To address this, a new force field for DVOCB(n) was developed largely using the TAFFI framework.[38] The TAFFI-gen force field demonstrated robust performance across small-molecule organics with parametrization solely from quantum chemistry data. Here, no experimental data were used for the parametrization. All requisite quantum chemical calculations were performed using density functional theory using ωB97X-D3[41,42]/def2-TZVP[43,44] with the ORCA package.[45] However, TAFFI-gen was necessarily extended in three ways to facilitate the simulation of DVOCB(n).

The first extension was to augment the standard approach to topological atom-typing. TAFFI formalized atom-typing using graph-theoretic principles. In TAFFI-gen, atom types were purely specified using covalent bonding connectivity with uniqueness determined out to a bond depth of two. Here, atom types were augmented to indicate the disposition of rings (*syn* and *anti*) for atoms associated with such structures and also whether atoms were in roughly equatorial or axial positions around the ring. This allows for a more flexible and expressive representation of the modeled atoms. To be otherwise consistent with TAFFI-gen, topological environments were still resolved to a bond depth of two.[38] A full list of derived atom types according to this procedure is provided in Table S1 of the Supporting Information.

The second extension was to regularize parametrization of charges for the newly devised atom types. In particular, partial charges were fit to minimize the objective function:

$$\chi_q^2 = \sum_s^{N_{samples}} (\omega_{pot} N_{pot}^{-1} \sum_i^{N_{pot}} (V_{QC,i} - V_{FF,i})^2 + \omega_D \sum_i^3 (D_{QC,i} - D_{FF,i})^2 + \omega_T (q_T - \sum_i^{N_{atoms}} q_i)^2 + \omega_r N_{atoms}^{-1} \sum_i^{N_{atoms}} (q_i - q_{r,i})^2) \quad (1)$$

In eq 1, the first three terms within the summation over all samples s are original to the TAFFI framework. These account for reproducing the electric potential, the molecular dipole, and the total charge of the molecule, and the last term penalizes large deviations in the charge of a reference atom of type $q_{r,i}$. The weighting coefficients used were ω_{pot} = 1.0, ω_D = 0.1, ω_T = 1.0, and ω_r = 0.1. This was motivated to promote consistency with charges previously determined for topologically equivalent atom types already present in TAFFI-gen. In addition, bulkier model compounds were required to fully represent distinguishing atomic environments for the ring molecules, and such large molecules can pose issues for determination of partial charges via approaches that fit electrostatic potentials, like the CHELPG[46] approach used in this work.

The third extension was to add new angle and dihedral potentials to model certain interactions for the enchained rings. A particular challenge for these strained ring systems is the substantial coupling between intramolecular modes, which cannot be captured by using the traditional OPLS-style functional forms employed in TAFFI-gen. This is addressed by formulating coupled angle-dihedral potentials as follows. Suppose that a ring is formed by atoms i, j, k, and l. We then let the minimum-energy angle formed between any two carbons i, j of the ring and a third atom i' (either a hydrogen or a carbon that is part of a different ring/terminal group) to be a function of the dihedral state of the ring (Supporting Information, Figure S16) to define

$$\theta_{i'ij}^{min} = \theta_{i'ij}^{(0)}(\phi_{ijkl}) \quad (2)$$

where $\theta_{i'ij}^{min}$ is the minimum-energy angle formed by atoms i, j, and i' and ϕ_{ijkl} is the dihedral angle formed by atoms i, j, k, and l. The minimum-energy angle is parametrized using a polynomial:

$$\theta_{i'ij}^{(0)}(\phi_{i'ijk}) = \sum_{m=0}^{3} c_m \phi_{i'ijk}^m \quad (3)$$

where the c_m are fitting coefficients. Then, the angular bending energy is modeled using a harmonic form

$$U_{bend}(\theta_{i'ij}, \phi_{i'ijk}) = K_{i'ij}[\theta_{i'ij} - \theta_{i'ij}^{(0)}(\phi_{i'ijk})]^2 \quad (4)$$

where $K_{i'ij}$ is a fitting coefficient. We note that $\phi_{i'ijk}$ and ϕ_{ijkl} are coupled and display a monotonic relationship (Supporting Information, Figure S16), so the use of the former is one of computational convenience. Finally, residual energetics associated with ring flipping were captured by using a tabular potential as a function of ϕ_{ijkl}. Additional details regarding the parametrization of these potentials are included in Section S5 of the Supporting Information.

Figure 2A compares reference DFT energies to those produced by different force fields as a function of the *syn* ring dihedral. Figure 2B shows the same comparison for an *anti* ring. With the aforementioned extensions, the newly parametrized force field (TAFFI-DVOCB) faithfully reproduces conformational energetics of ring flipping with quantum chemical (DFT) accuracy. By contrast, both OPLS-AA and TAFFI-gen exhibit notable deviations from DFT predictions for both *syn* and *anti* isomers. These deviations motivate the additional complexity of parametrizing a bespoke force field for DVOCB, although the general strategy may be extended to other ring-based systems.

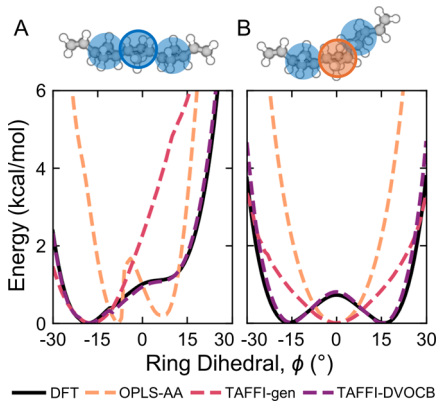

Figure 2. Comparison of ring-flipping energetics in DVOCB(n) with different theoretical treatments. The energy of a DVOCB(3) oligomer as a function of the central ring dihedral for (A) a *syn-syn-syn* arrangement of rings and (B) a *syn-anti-syn* arrangement of rings. The ring dihedral is defined as the dihedral formed by four carbon atoms in the ring. DFT results are geometry optimized using the ωB97X-D3[41,42]/def2-TZVP[43,44] level of theory. Data for the OPLS-AA force field[40] and the general topology-automated force-field interactions (TAFFI-gen) approach[38] reflect energies calculated with configurations optimized using DFT. TAFFI-DVOCB energy surfaces are calculated using our new force field. Dihedral constrained energy minimizations are performed with the TAFFI-DVOCB force field. The energy surfaces after energy minimizations are plotted.

https://doi.org/10.1021/acs.chemmater.4c02576
Chem. Mater. 2024, 36, 11596−11605

2.2.3. Simulated X-ray Scattering Profiles. Simulated scattering intensities were obtained based on the virtual diffraction algorithm.[47] First, a set of reciprocal lattice vectors $\mathbf{k}$ was generated,

$$\mathbf{k} = \left(\frac{N_x}{l_x}, \frac{N_y}{l_y}, \frac{N_z}{l_z}\right) \tag{5}$$

where N_x, N_y, and N_z are integers and l_x, l_y, and l_z are the simulation box lengths. Second, the corresponding scattering angle θ_s was calculated by

$$\theta_s = \arcsin(\|\mathbf{k}\|\lambda/2) \tag{6}$$

where λ = 1.541838 Å is the average wavelength of a Cu K-α X-ray and $\|\mathbf{k}\|$ is the Euclidean norm on $\mathbf{k}$; the maximum $\|\mathbf{k}\|$ examined is 3 Å^{-1}. Third, the structure factor $F(\mathbf{k})$ was calculated as

$$F(\mathbf{k}) = \sum_{j=1}^{N} f_j(\theta_s)\exp(2\pi i\mathbf{k}\cdot\mathbf{r}_j) \tag{7}$$

where $\mathbf{r}_j$ is the Cartesian position of atom j with an angle-dependent atomic scattering factor[48] $f_j(\theta_s)$, and N is the number of atoms in the simulation cell. Note that the periodic image of atoms will give the same structure factor; therefore, it is not necessary to translate the position of atoms. Fourth, the scattering intensity was subsequently computed as

$$I(\mathbf{k}) = L_p(\theta_s)\cdot\frac{F(\mathbf{k})F^*(\mathbf{k})}{N} \tag{8}$$

where "*" denotes the complex conjugate and

$$L_p(\theta_s) = \frac{1 + \cos^2(2\theta_s)}{\cos(\theta_s)\sin^2(\theta_s)} \tag{9}$$

is the Lorentz-polarization factor. Finally, the computed set of $I(\mathbf{k})$ is smoothed by Gaussian functions

$$I(q) = \sum_{\mathbf{k}} I(\mathbf{k})\exp\left(-\frac{(q - \|\mathbf{k}\|)^2}{2\sigma^2}\right) \tag{10}$$

where the wavevector q is sampled as uniformly distributed points and σ = 0.016 Å^{-1} is used for comparison to experimental results.

2.2.4. Chain-Segment Orientation. For DVOCB(n), chain segments were defined as each cyclobutyl ring. The orientation of the segment $\vec{\alpha}$ was defined as the sum of four carbon−carbon bond vectors (oriented toward the central carbons). Denoting the carbons as i, j, k, and l with j and l as the central carbons, then $\vec{\alpha} = \sum_{a\in\{i,k\}}\sum_{b\in\{j,l\}}(\mathbf{r}_b - \mathbf{r}_a)$. For n-alkanes, chain segments of similar length were defined using groups of three consecutive backbone carbons, the orientation of this group then being the sum of two carbon−carbon bond vectors (oriented toward the central carbon). Denoting the carbons as i, j, and k with j as the central carbon, then $\vec{\alpha} = \sum_{a\in\{i,k\}}(\mathbf{r}_j - \mathbf{r}_a)$.

2.2.5. Parallel Order Parameter. To characterize the crystal structure of DVOCB(n) systems at low temperatures, we define an order parameter to detect whether chains are oriented in a parallel fashion. The approach is inspired by previous works on n-alkane systems.[26,28] The order parameter P is obtained as follows. First, chain-segment orientations are summed for each chain to obtain a chain orientation, denoted as

$$\vec{\beta}_i = \sum_{\nu=2}^{n-1}(-1)^{\nu}\vec{\alpha}_{\nu}^{i} \tag{11}$$

where n is the number of segments of chain i, $\vec{\alpha}_{\nu}^{i}$ is the orientation of the νth segment on chain i, and the $(-1)^{\nu}$ term is included because neighboring segments tend to have opposite orientations; the two end rings are excluded because of their additional conformational entropy. Second, a local order parameter is defined by considering its orientation relative to its six nearest-neighbor chains. The relative orientations of chains i and j are characterized using

$$\cos\theta_{ij}^{(\beta)} \equiv (\vec{\beta}_i - \vec{\beta}_i\cdot\hat{y}\hat{y})\cdot(\vec{\beta}_j - \vec{\beta}_j\cdot\hat{y}\hat{y}) \tag{12}$$

which relates to the angle formed between the two chain-orientation vectors as projected onto the xz plane. Subsequently, the local order parameter for chain i is obtained via

$$p_i = \prod_{j\in\mathcal{N}(i)} H(\cos\theta_{ij}^{(\beta)} - \cos\theta_{\max}) \tag{13}$$

where $\mathcal{N}(i)$ denotes the local neighborhood of i (i.e., the six nearest-neighbor chains), $H(\cdot)$ denotes the Heaviside step function, and $\theta_{\max}$ is a threshold angle. The result of eq 13 is that p_i is equal to unity if all of the θ_{ij} values are within $\theta_{\max}$ and zero otherwise. For analysis within the main text, we set $\cos\theta_{\max} = \pi/4$ or 45°; using smaller $\theta_{\max}$ results in smaller p_i but does not influence any trends. Finally, the system order parameter is obtained as the average of all the local order parameters

$$P = \frac{1}{N_c}\sum_{i}^{N_c} p_i \tag{14}$$

where N_c is the number of chains in the system. We also calculated order parameters for n-alkane systems using the same approach (see Supporting Information, Section S7), which agrees with previous studies.[26,28]

2.2.6. Rotational Segmental Dynamics. To characterize the rotational dynamics of chains, we calculated the characteristic relaxation times required for decorrelation of chain-segment orientations. The autocorrelation function of chain-segment orientation $\vec{\alpha}(t)$ was calculated and fitted as

$$C_{\alpha,\alpha}(t) = \langle\vec{\alpha}(0)\cdot\vec{\alpha}(t)\rangle \tag{15}$$

$$\approx(1 - A)\exp[-(t/t_1)] + A\exp[-(t/t_2)^{\beta}] \tag{16}$$

where A, t_1, t_2, and β are fitting parameters. In eq 16, the first exponential term is intended to capture short-time motions, while the second stretched-exponential term captures relaxations for more collective chain rearrangements. The characteristic relaxation time follows as

$$\langle\tau\rangle = (1 - A)t_1 + At_2\beta^{-1}\Gamma(\beta^{-1}) \tag{17}$$

where $\Gamma(\cdot)$ indicates the Gamma function. Characteristic relaxation times for both *anti* and *syn* rings were obtained by averaging data resolved by those assignments.

2.2.7. Detailed Structural Analysis. To characterize structural correlations along polymer chains, we calculated two distribution functions associated with the orientation of the chain segments. In analogy to eq 12, we obtain the angle between an arbitrary unit vector $\hat{r}$ perpendicular to the chain axis and the chain-segment orientation, both projected onto the xz plane. As $\hat{r}$ is an arbitrary reference, we select $\hat{x}$, which yields

$$\cos\theta_i^{(\alpha)} \equiv (\vec{\alpha}_i - \vec{\alpha}_i\cdot\hat{y}\hat{y})\cdot\hat{x} \tag{18}$$

Subsequently, we generated the two-dimensional joint probability distribution for neighboring chain segments, $P(\theta_i^{(\alpha)}, \theta_{i+1}^{(\alpha)})$. To examine correlations across the chain, we also examined the distribution of orientation differences between chain ends, $P(\theta_1^{(\alpha)} - \theta_n^{(\alpha)})$.

3. RESULTS AND DISCUSSION

3.1. Experimental Characterization of Structural Transitions in DVOCB(n). Structural transitions consistent with a crystal-to-rotator phase transition are consistently observed in the DVOCB(n) systems. Figure 3A illustrates characteristic features through in situ variable-temperature WAXS on DVOCB(10). When the sample is heated, the X-ray scattering profile exhibits a transition from two peaks, labeled as b and c, to one peak, labeled as d; the two-to-one peak

https://doi.org/10.1021/acs.chemmater.4c02576
Chem. Mater. 2024, 36, 11596−11605

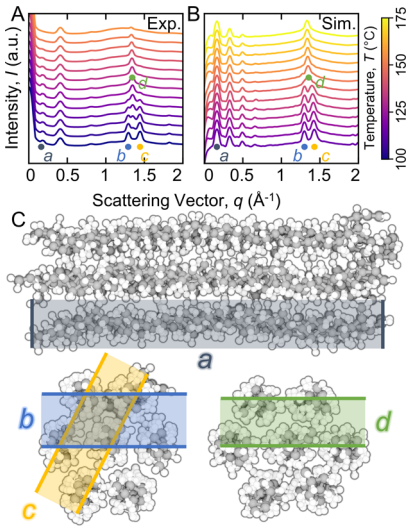

Figure 3. Structural characterization of DVOCB(10). (A) Experimental in situ heating of WAXS data as a function of heating. The temperature interval between curves is 4.6 °C. (B) Simulated X-ray scattering data as a function of heating. The temperature interval between curves is 5 °C. In panels (A) and (B), four prominent peaks are labeled as *a* (dark blue), *b* (light blue), *c* (yellow), and *d* (green) for ease of visual identification. The intensities in both panels are on a logarithmic scale. Both panels share the color bar on the right. (C) Visualization of simulation configurations for interpretation of the locations of prominent peaks in (A) and (B). The top-down view depicts the distance at *a*, which corresponds to an end-to-end distance of the oligomer. The side-on view depicts relevant distances for *b*, *c*, and *d*, which correspond to interchain packing distances along different directions.

transition is observed around 125 °C near q = 1.4 Å^{-1}. The two-peak feature is ascribed to a crystalline phase, whereas the one-peak feature is associated with a prospective rotator phase. At high enough temperatures, the single peak gradually dissipates, signifying the onset of melting into an amorphous state. We note that the strong peak observed at q = 0.45 Å^{-1} is the Kapton peak from the mounting windows used in the sample preparation. During the transition, three peaks are shown near q = 1.4 Å^{-1}. These three peaks are at the same positions as peaks *b*, *c*, and *d*, suggesting coexisting crystal and rotator phases. This observation is supported by DSC measurements of experimental samples (Supporting Information, Figure S12) that indicate a broad temperature range of the crystal-to-rotator phase transition, which we partially attribute to dispersity effects. Similar observations can be made for DVOCB(n) of other oligomer lengths (Supporting Information, Figure S10). This progression is similar to that observed in *n*-alkanes, which possess well-known crystal-to-rotator phase transitions.[19]

There are two notable differences between the structural progression of DVOCB(n) and *n*-alkanes. First, DVOCB(n) exhibits a relatively larger stability window for its prospective rotator phase. For DVOCB(10), this phase persists within a window of ca. 40 °C before melting. By contrast, an *n*-alkane with a similar chain length (e.g., $C_{30}H_{62}$) possesses a stability window for a rotator phase that is smaller than 10 °C.[19] Second, observing prospective rotator phases in the DVOCB(n) family is not restricted to smaller oligomers and molecular weights. Here, we study the behavior of shorter DVOCB(n) oligomers (M_n < 500 g/mol); however, similar features are observed in the context of chain-extended systems of much higher molecular weights (M_n > 40,000 g/mol),[33] though these systems are not precise equivalents of simply replicating DVOCB(n) to higher molecular weights. By contrast, reported rotator phases of *n*-alkanes have been limited to much lesser molecular weights (M_n ≈ 1000 g/mol).[1,49] Together, these differences suggest that the prospective rotator phases of DVOCB(n) may have characteristically distinct manifestations relative to those of *n*-alkanes despite both having significant shared chemistry.

3.2. Elucidation of the DVOCB(n) Structure across Phases. To understand the emergence and characteristics of the prospective rotator phases in DVOCB(n), we used MD simulations to ascertain the real-space structural features that underlie the experimental X-ray scattering data. Figure 3B illustrates that simulations produce a structural progression upon heating similar to that of the experiments. In particular, the four previously noted prominent peaks of the experimental measurements, *a*, *b*, *c*, and *d*, are also observed in simulated scattering intensities at similar wavevectors (Supporting Information, Figure S17). This similarity enables assignment of the peaks to different types of molecular-level organization. The peaks at around q = 0.45 Å^{-1} arise from higher-order reflections of peak *a*, as indicated in eq 7. Figure 3C depicts simulation configurations that convey a real-space interpretation. We find that the DVOCB(n) tends to form layered, lamellar structures with widths oriented along the longitudinal chain axis. Peak *a* is consistent with the distance between such layers (Figure 3C, top), which is similar between both the crystal and rotator phases for a given n. The peaks *b* and *c* correspond to two different in-plane distances between DVOCB chains within the ordered lamellae at low temperatures, which reflects a stretched hexagonal (orthorhombic) packing of aligned chains. The peak *d* also corresponds to a single distance in the plane of the lamellae, which reflects a more isotropic hexagonal packing.

Figure 4A shows that the positions of prominent peaks also exhibit notable temperature and molecular-weight dependence. At a fixed molecular weight or oligomer length n, the increasing temperature tends to shift the positions of peaks *c* and *d* to smaller values; the *a* and *b* peaks are not strong functions of temperature. Thermal expansion (increasing chain entropy) should tend to shift all peaks to lower q, while the shift toward hexagonal packing moves *b* and *c* closer. The combination of these effects results in a roughly static position of *b*. Thermal expansion of the material first relaxes the anisotropic hexagonal packing before more generally increasing chain entropy. As molecular weight increases, peaks progress in a similar fashion but at higher temperatures. The collapse of peaks *b* and *c* to *d* occurs at higher temperatures for longer oligomers. In addition, the peaks surrounding these transitions are shifted to relatively smaller q values for longer oligomers. This is most evident for peak *a*, which simply relates to larger lamellae owing to longer chains but remains true for other features. Conversely, peak positions that correspond to interchain packing distances generally shift to higher q when comparing oligomers of increasing length at the same temperature. This suggests that the chains pack more closely for longer oligomers, which is expected from the reductions in conformational entropy at the chain ends.

The trends of Figure 4A are largely consistent with additional experimental WAXS. Direct comparisons of peak positions between simulations and experiments are shown in

https://doi.org/10.1021/acs.chemmater.4c02576
Chem. Mater. 2024, 36, 11596−11605

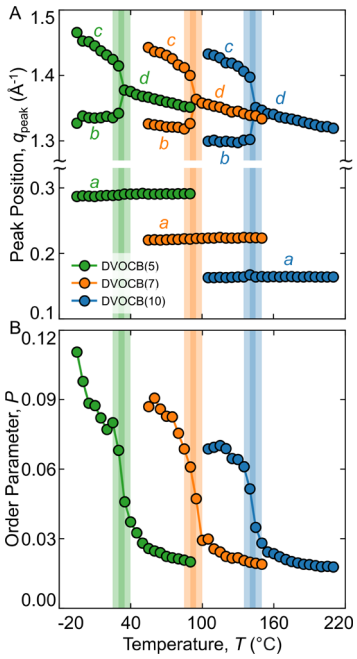

Figure 4. Observations of the rotator phase transition in DVOCB(n) systems. (A) Simulated X-ray peak positions of DVOCB oligomers as a function of temperature. The top part tracks peaks *b*, *c*, and *d*, while the bottom part tracks peak *a*. (B) Parallel order parameter P of DVOCB oligomers is a function of temperature. The shadow regions indicate when the phase transition happens.

Supporting Information, Section S6. There are two main disparities. First, the transition temperatures are consistently higher in the simulations compared to the experimental measurements. Second, the experimental data often possess peaks corresponding to coexisting crystal and rotator phases over a short temperature interval preceding the collapse to a single peak indicative of the rotator phase. In part, both differences may be due to chain-length dispersity and the presence of coexisting amorphous material in the experimental samples (see Supporting Information, Section S8). Simulations including dispersity in oligomer length yield lower transition temperatures. However, there may also be kinetic limitations of the simulations; such factors are often notable in determination of glass-transition temperatures.[50] Finally, the TAFFI-DVOCB force field employed may also possess errors in certain properties, as it is not tuned to reproduce any specific experimental observable. Because our intent is not to precisely determine crystal-to-rotator transition temperatures but rather to elucidate the characteristics thereof, the overall similarity between Figure 3A and B provides confidence in the interpretation built from the MD simulation.

Importantly, the two-to-one peak transition is captured well by a structural order parameter that captures the rotational disorder of the DVOCB(n) chains. We designed the order parameter P to decay if nearby chains are not similarly oriented in directions orthogonal to their longitudinal axis (see eqs 11−14); the approach is inspired by previous *n*-alkane studies.[26,28] Figure 4B shows that P markedly decreases precisely at the temperature of the two-to-one peak collapse. Consequently, we conclude that this feature indeed reflects a crystal-to-rotator phase transition, with the latter characterized by the enhanced rotational disorder of longitudinally aligned chains. In addition, the enhanced similarity in chain orientations in tandem with the geometry of the four-carbon enchained rings in DVOCB(n) gives rise to different interchain distances that relate to peaks *a* and *b*.

3.3. Dynamical Characteristics of DVOCB(n) across Phases. Having established the presence of prospective rotator phases in DVOCB(n), we now elucidate what molecular features distinguish its transition relative to those of *n*-alkane systems. Figure 5A,B compares the rotational dynamics of chain segments of DVOCB(10) and its *n*-alkane analogue, $C_{31}H_{64}$, via the autocorrelation of chain-segment orientations. In DVOCB(10), the autocorrelation function generally exhibits an initial rapid decay (below 0.6) followed

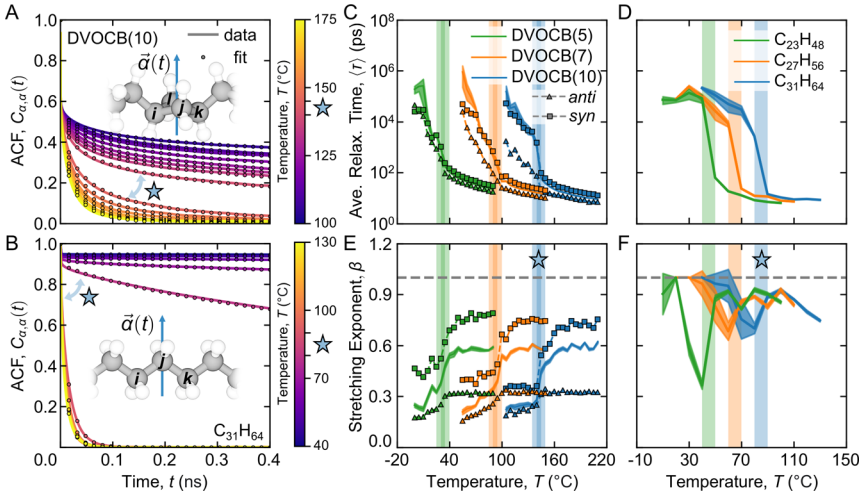

Figure 5. Comparison of segmental dynamics between DVOCB oligomers and *n*-alkane systems. (A,B) Orientation autocorrelation function of (A) DVOCB(10) and (B) $C_{31}H_{64}$ at a series of different temperatures. The structure diagrams of chain section orientation, $\vec{\alpha}(t)$, in DVOCB oligomers and *n*-alkane chains are inset. Note that the solid lines indicate simulation results and markers indicate specific values for the best-fit curves. (C,D) Average chain relaxation times $\langle\tau\rangle$ versus temperature for DVOCB oligomers and *n*-alkanes. (E,F) Stretching exponent β versus temperature for DVOCB oligomers and *n*-alkanes. The shaded regions in (C−F) indicate statistical uncertainties that reflect the standard error of the mean as estimated from bootstrap resampling. The dashed line in parts (E) and (F) indicates the β = 1 position. The pentagram markers highlight the region closest to the transition temperature.

https://doi.org/10.1021/acs.chemmater.4c02576
Chem. Mater. 2024, 36, 11596−11605

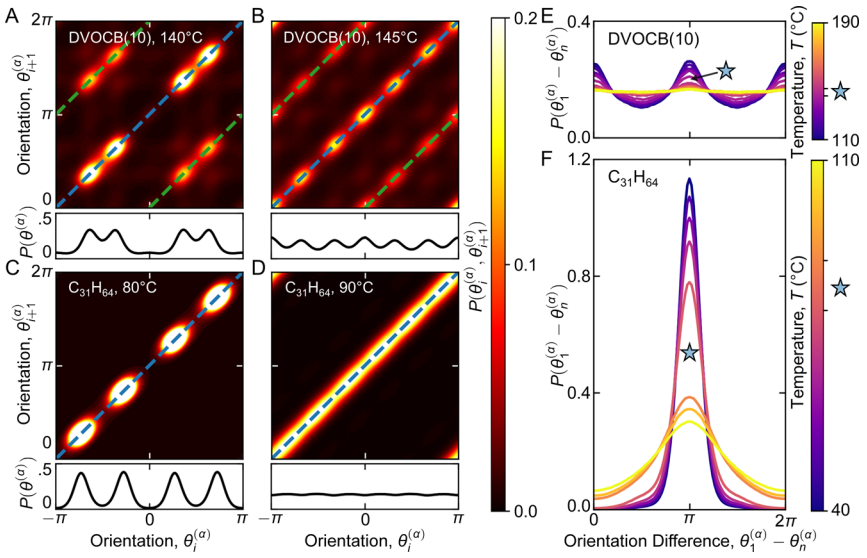

Figure 6. Comparison of the orientation independence of the same chain sections between DVOCB(n) and n-alkane systems. (A,B) Orientation distribution of two consecutive rings and single rings on the DVOCB(10) chains at 140 °C (crystal phase) and 145 °C (rotator phase). The green dashed lines highlight conditions where two consecutive rings have the same orientation, and the blue dashed lines indicate that such rings have opposing orientations. $\theta^{(\alpha)}$ is the scaled orientation of $\vec{\alpha}$ on the xy plane, which uses the x direction as a reference. (C,D) Orientation distribution of two consecutive sections and single sections on $C_{31}H_{64}$ chains is at 80 °C (crystal phase) and 90 °C (rotator phase). The blue dashed lines indicate that two consecutive sections have opposing orientations. (E,F) Probability distributions of two end segments' orientation difference on DVOCB(10) chains and $C_{31}H_{64}$ chains in temperature series. The pentagram markers highlight the region closest to the transition temperature.

by a gradual relaxation. The initial fast relaxation relates to the local oscillation of ring orientation and especially the ring-flipping behavior, which persist even below the crystal-to-rotator phase transition temperature. The secondary relaxation is attributed to actual segmental rotation, which results in the two groupings of data separated by a clear gap notated by the pentagram in Figure 5A. In $C_{31}H_{64}$, local fluctuations in orientation are substantially restricted below the crystal-to-rotator phase transition temperature, resulting in the rapid initial decrease to a much larger correlated value of 0.95. Subsequently, longer time relaxations set in only at elevated temperatures; the difference between relaxation processes below and above their respective crystal-to-rotator phase transition temperatures is more stark in $C_{31}H_{64}$ than in DVOCB(10), as indicated by a more obvious change notated by the pentagram in Figure 5B. Other simulated DVOCB(n) and n-alkane chains have similar behaviors as DVOCB(10) and $C_{31}H_{64}$ (Supporting Information, Figure S24). These results illustrate that the enchained rings of DVOCB(n) give rise to dynamically distinct behavior relative to that of n-alkanes.

Figure 5C,D reveals that DVOCB(n) and their analogous n-alkanes also display distinct temperature-dependent relaxation behaviors. As the temperature increases for DVOCB(n) (Figure 5C), average relaxation times for chain-segment rotation decrease in the crystal phase, drop dramatically around the crystal-to-rotator transition, and then decrease at a slower rate in the rotator phase. By resolving contributions of the distinct geometric isomers, we find that rotational decorrelation of *syn* rings is consistently slower than that of *anti* rings. The faster decorrelation of *anti* rings is attributed to their lower and symmetric barrier to ring flipping (Figure 2B). As the temperature increases for the n-alkanes (Figure 5D), there are again roughly three regimes of behavior. While relaxation times dramatically drop around the crystal-to-rotator transition temperature indicated by vertical shaded regions, the relaxation times are comparatively more constant on either side relative to DVOCB(n). Thus, while the sudden shift in relaxation times in n-alkanes is more or less coincident with the observed structural transition temperature, the results for DVOCB(n) suggest a more gradual onset of rotational disorder that precedes the major structural changes, deduced from the scattering and order-parameter analyses in Section 3.2, which are associated with a phase transition. Importantly, the relaxation times in both systems near the transition temperature are on the order of nanoseconds, which can be reliably converged and attributed to equilibrium characteristics of the system rather than kinetic effects.

Figure 5E,F provides insight into temperature-dependent behavior by examining stretching exponents, β, for the average relaxation times (eq 17). Whereas β of DVOCB(n) systems gradually increase, the n-alkane systems display nonmonotonic behavior that cumulatively decreases β from the crystalline to the rotator phase. Additionally, β is generally significantly lower in DVOCB(n) compared to n-alkanes. When $\beta = 1$, the stretched exponential becomes a simple exponential with a single characteristic time scale. Negative deviations of β from unity indicate a range of relaxation processes without a single characteristic time scale. Thus, this observation suggests that n-alkanes have more well-defined relaxation phenomena, while DVOCB(n) exhibits a series of thermally activated processes, which is supported by the broader distribution of single-ring relaxation (Supporting Information, Figure S25). The β for n-alkanes interestingly decreases during the temperature interval preceding the crystal-to-rotator phase transition indicated by the vertical shaded region in Figure 5F. We posit this arises as the orientations of groups of chains, of increasing size, begin to decouple. Conversely, relaxation processes for DVOCB(n) become more uniform as the temperature increases. Therefore, crystal-to-rotator phase transitions in DVOCB(n) are governed by processes with varied time scales that promote rotational disorder, whereas n-alkane transitions depend on phenomena with more uniform relaxation times.

https://doi.org/10.1021/acs.chemmater.4c02576
Chem. Mater. 2024, 36, 11596−11605

Combining experimental and simulation results on both structural and dynamical characteristics of DVOCB(n) confirms a crystal-to-rotator phase transition, marked by a shift from orthorhombic crystal packing to an isotropic hexagonal lattice of rotationally disordered chains.

3.4. Contributions of Enchained Rings. We hypothesized that the distinct dynamical characteristics of DVOCB(n) relaxation processes relative to n-alkanes must be due to contributions of the enchained rings. To better understand the implications of their presence, we compare different spatial correlations of chain-segment orientations with those of n-alkanes.

Figure 6A,B examines the correlation of nearest-neighbor chain-segment orientations in DVOCB(10) below and above the crystal-to-rotator transition temperature through the joint probability distributions. Across both temperatures, there are multiple distinct high-probability regions located in diagonal bands; the positioning of the diagonal bands indicates that neighboring chain segments are aligned in either the same (green dashed lines) or opposing (blue dashed lines) directions. A primary distinction between the crystal and the rotator phase is that the latter possesses near-continuous bands, while the crystal phase presents more restrictions on the conformation. In the crystal phase, four orientations ($\pm\pi/3$ and $\pm2\pi/3$) are favored, which correspond to parallel orientations in the hexagonal lattice. In the rotator phase, high-probability regions are connected and feature all six orientations along the hexagonal lattice; however, there are still visually distinct populations. These populations can be readily discerned from the marginal plot, which depicts the univariate probability distribution of chain-segment orientations. DVOCB(5) and DVOCB(7) also exhibit similar behaviors (Supporting Information, Figure S26). The major features of Figure 6A,B can be obtained by presuming chain-segment orientations are statistically independent. However, contrast with the empirical joint probability distribution (Supporting Information, Figure S27) illustrates that chain segments in both crystalline and rotator phases of DVOCB(n) are locally correlated, but each enchained ring can access multiple configurational states.

Figure 6C,D repeats the analysis from Figure 6A,B for the analogous n-alkane $C_{31}H_{64}$, which shows markedly different behavior compared to DVOCB(10). In the crystalline phase, nearest-neighbor chain-segment orientations are highly correlated and restricted to four primary orientations ($\pm\pi/4$ and $\pm3\pi/4$), which derive from the orthogonal structure of the n-alkane crystal phase. All statistical populations of the joint probability distribution are restricted to a single diagonal, which implies that nearest-neighbor segments share the opposite orientation (blue dashed lines in Figure 6C). In the rotator phase, the probability regions become continuous bands restricted to the diagonal. This implies that more orientations are accessible, but nearest-neighbor orientations remain highly correlated. The univariate probability distribution indicates a nearly uniform distribution with slight enhancements around six orientations that reflect the underlying hexagonal lattice. Other simulated n-alkane chains show the same behaviors (Supporting Information, Figure S26). For $C_{31}H_{64}$, assuming independent chain-segment orientations is highly erroneous (Supporting Information, Figure S27), as the orientation of one segment effectively determines the next.

The extent of correlation between neighboring chain segments in DVOCB(n) compared to n-alkanes leads to disparate behavior at larger length scales. This is illustrated in Figure 6E,F, which show the distribution of chain-end orientation differences as a function of temperature for DVOCB(10) and $C_{31}H_{64}$. For DVOCB(10), two peaks at 0 and π are discernible at low temperatures, suggesting some global orientational preference for the chain. These peaks diminish with increasing temperature, leading to a uniform distribution, indicating that correlations do not persist over the entire chain. For $C_{31}H_{64}$, there is a single peak at π that is discernible across all temperatures. This indicates that relative orientations of chain ends are restricted and that chain-segment orientation correlations persist over the entire chain.

Altogether, our results implicate the rotational entropy of the enchained-ring architecture as being responsible for the contrasting behavior of DVOCB(n) relative to n-alkanes. From Figure 6, we conclude that rings across the chain rotate semi-independently from one another. While there are local correlations, the manifestations are more varied than in n-alkanes and increasingly diminish upon heating. This latter aspect also explains why there is a mixture of temperature-dependent relaxation processes in Figure 5, as thermal energy permits more chain segments to break free of restricted rotations. Furthermore, we posit that individual rings promoting rotational disorder at the segment level allow rotator phases to exist within DVOCB-based systems of higher molecular weights, although the size of the crystal stems may still be limited by oligomer size.[33] By contrast, chain-segment orientations are more homogeneous within a chain for n-alkanes such that chain rotation is a cooperative effect. This limits relaxation processes to either whole-chain rotations or interchain phenomena and restricts observation of rotator phases to oligomeric n-alkane systems.

4. CONCLUSIONS

We combined experimentation and MD simulation to characterize and elucidate observed rotator phases in a family of chemically recyclable (1,n'-divinyl)oligocyclobutanes or DVOCB(n). The theoretical study of DVOCB(n) was supported by nuanced force-field development to address its unique enchained-ring architecture. Subsequent modeling was able to reproduce and elucidate structural features observed from in situ WAXS. In particular, the two-to-one peak collapse associated with the crystal-to-rotator phase transitions corresponds to a shift from a stretched to an isotropic hexagonal lattice packing, while a persistent prominent peak corresponds to the longitudinal length scale of lamellae. Beyond this structural characterization, simulation analyses demonstrated that DVOCB(n) systems are dynamically distinct from analogous n-alkanes. The molecular origins of such differences were attributed to semi-independent rotation of the enchained rings. This leads to more varied relaxation processes and less overall correlation of chain-segment orientations relative to n-alkanes. We posit that this architectural difference underlies the larger stability window for rotator phases of DVOCB(n) as well as the presence of rotator phases in higher molecular weight, chain-extended DVOCB systems.[33] The broader temperature range of the rotator phase may make DVOCB(n) appealing for certain applications, such as phase-change materials.[51]

While this study focused on a specific class of materials, its insights and methods have broader implications. This work also provides a dynamic analysis of crystal-to-rotator phase transitions in n-alkanes, which has not been previously

https://doi.org/10.1021/acs.chemmater.4c02576
Chem. Mater. 2024, 36, 11596−11605

reported. The described order parameter for characterizing crystal-to-rotator phase transitions in DVOCB(n) can also be easily applied to future systems. Our tailored extension of TAFFI-gen lays a foundation for generally expanding the TAFFI framework to address stereochemistry and ring systems. In the future, it may be interesting to apply similar analyses to other ring-containing systems with rotator phases, such as chain-extended DVOCB[33] and hydrogenated polynorbornene.[17,18,52]

■ ASSOCIATED CONTENT

Supporting Information

The Supporting Information is available free of charge at https://pubs.acs.org/doi/10.1021/acs.chemmater.4c02576.

Wide-angle and small-angle X-ray scattering; differential scanning calorimetry; DVOCB(8) repeat sample WAXS; system preparation and production; DVOCB(n) parametrization; comparison of experimental and simulated X-ray scattering peaks; order parameters for n-alkane systems; simulated melting temperature dependencies; additional orientation autocorrelation analysis; and additional orientation correlation analysis (PDF)

■ AUTHOR INFORMATION

Corresponding Author

Michael A. Webb − *Department of Chemical and Biological Engineering, Princeton University, Princeton, New Jersey 08544, United States;* orcid.org/0000-0002-7420-4474; Email: mawebb@princeton.edu

Authors

Hang Zhang − *Department of Chemistry, Princeton University, Princeton, New Jersey 08544, United States*

Shawn M. Maguire − *Department of Chemical and Biological Engineering, Princeton University, Princeton, New Jersey 08544, United States;* orcid.org/0000-0002-5317-4990

Cherish Nie − *Department of Chemistry, Princeton University, Princeton, New Jersey 08544, United States;* orcid.org/0000-0002-3758-9950

Rodney D. Priestley − *Department of Chemical and Biological Engineering, Princeton University, Princeton, New Jersey 08544, United States;* orcid.org/0000-0001-6765-2933

Paul J. Chirik − *Department of Chemistry, Princeton University, Princeton, New Jersey 08544, United States;* orcid.org/0000-0001-8473-2898

Richard A. Register − *Department of Chemical and Biological Engineering, Princeton University, Princeton, New Jersey 08544, United States;* orcid.org/0000-0002-5223-4306

Emily C. Davidson − *Department of Chemical and Biological Engineering, Princeton University, Princeton, New Jersey 08544, United States;* orcid.org/0000-0001-5819-9233

Complete contact information is available at: https://pubs.acs.org/10.1021/acs.chemmater.4c02576

Notes

The authors declare no competing financial interest.

■ ACKNOWLEDGMENTS

This research was supported by the U.S. Department of Energy, Office of Science, Office of Basic Energy Sciences, Catalysis Science program, under award DE-SC0022303. Simulations and analyses were performed using resources from Princeton Research Computing at Princeton University, which is a consortium led by the Princeton Institute for Computational Science and Engineering (PICSciE) and the Office of Information Technology's Research Computing. S.M.M. thanks Yejoon Seo and Sahana Sundar for Flash DSC guidance and X-ray assistance, respectively. Additionally, S.M.M. thanks Alice S. Fergerson and Chun Lam Clement Chan for help with Linkam temperature calibrations. The authors acknowledge the use of Princeton's Imaging and Analysis Center (IAC) for X-ray analysis conducted in this work. The IAC is partially supported through the Princeton Center for Complex Materials (PCCM), a National Science Foundation (NSF)-MRSEC program (DMR-2011750).

■ REFERENCES

(1) Snyder, R. G.; Maroncelli, M.; Qi, S. P.; Strauss, H. L. Phase Transitions and Nonplanar Conformers in Crystalline n -Alkanes. *Science* **1981**, *214*, 188−190.

(2) Hu, W.; Srinivas, S.; Sirota, E. B. Crystalline Structure and Properties of EP and EB Copolymers by Solid-State NMR, DSC, and WAXS. *Macromolecules* **2002**, *35*, 5013−5024.

(3) Imanishi, Y.; Naga, N.; Tsubooka, M. Synthesis of polyolefins with unique properties by using metallocene-type catalysts. *Macromol. Symp.* **2003**, *195*, 45−62.

(4) Pirro, D. M.; Daschner, E. In Lubrication Fundamentals; Wessol, A., Ed.; CRC Press, 2001; DOI: .

(5) Denkov, N.; Tcholakova, S.; Lesov, I.; Cholakova, D.; Smoukov, S. K. Self-shaping of oil droplets via the formation of intermediate rotator phases upon cooling. *Nature* **2015**, *528*, 392−395.

(6) Small, D. M. *The Physical Chemistry of Lipids*; Springer US, 1986; DOI: .

(7) Francis, W. *Fuels and fuel technology*, second ed.; Pergamon Press: Oxford, England, 1980; Description based on print version record.

(8) Sharma, A.; Tyagi, V.; Chen, C.; Buddhi, D. Review on thermal energy storage with phase change materials and applications. *Renewable and Sustainable Energy Reviews* **2009**, *13*, 318−345.

(9) Mukherjee, P. K. Phase transitions among the rotator phases of the normal alkanes: A review. *Phys. Rep.* **2015**, *588*, 1−54.

(10) Cholakova, D.; Tsvetkova, K.; Tcholakova, S.; Denkov, N. Rheological properties of rotator and crystalline phases of alkanes. *Colloids Surf., A* **2022**, *634*, No. 127926.

(11) Sirota, E. B.; King, H. E. J.; Shao, H. H.; Singer, D. M. Rotator Phases in Mixtures of n-Alkanes. *J. Phys. Chem.* **1995**, *99*, 798−804.

(12) Singh, S. Phase transitions in liquid crystals. *Phys. Rep.* **2000**, *324*, 107−269.

(13) Goodby, J. W.; Vill, V.; Collings, P. J.; Gleeson, H.; Kato, T. *Handbook of Liquid Crystals*; Wiley-VCH Verlag GmbH, 2014; p 5240.

(14) Thomsen, T.; Zachmann, H. G.; Kricheldorf, H. R. Investigation of the high-temperature phase transition of PHB/3-CI-PHB copolyester by means of deuteron NMR. *Journal of Macromolecular Science, Part B* **1991**, *30*, 87−99.

(15) Martínez Casado, F. J.; García Pérez, M. V.; Redondo Yélamos, M. I.; Rodríguez Cheda, J. A.; Sánchez Arenas, A.; López-Andrés, S.; García-Barriocanal, J.; Rivera, A.; León, C.; Santamaría, J. Intermediate Rotator Phase in Lead(II) Alkanoates. *J. Phys. Chem. C* **2007**, *111*, 6826−6831.

(16) Kaji, H.; Horii, F. Investigation of Dynamics of Poly-(dimethylsilane) in the Mesophase by Solid-State 29Si NMR: Evidence for Rotator Phase. *Macromolecules* **2007**, *40*, 5420−5423.

(17) Bishop, J. P.; Register, R. A. The crystal-crystal transition in hydrogenated ring-opened polynorbornenes: Tacticity, crystal thickening, and alignment. *J. Polym. Sci., Part B: Polym. Phys.* **2011**, *49*, 68−79.

(18) Klein, J. P.; Gdowski, Z. M.; Register, R. A. Controlling thermomechanical behavior of semicrystalline hydrogenated polynorbornene through the *cis*- to *trans*-cyclopentylene ratio. *J. Polym. Sci.* **2022**, *60*, 266−275.
(19) Sirota, E. B.; King, H. E.; Singer, D. M.; Shao, H. H. Rotator phases of the normal alkanes: An x-ray scattering study. *J. Chem. Phys.* **1993**, *98*, 5809−5824.
(20) Cholakova, D.; Denkov, N. Rotator phases in alkane systems: In bulk, surface layers and micro/nano-confinements. *Adv. Colloid Interface Sci.* **2019**, *269*, 7−42.
(21) Sirota, E. B.; Singer, D. M. Phase transitions among the rotator phases of the normal alkanes. *J. Chem. Phys.* **1994**, *101*, 10873−10882.
(22) Sirota, E. B.; Herhold, A. B. Transient Phase-Induced Nucleation. *Science* **1999**, *283*, 529−532.
(23) Ryckaert, J.-P.; McDonald, I. R.; Klein, M. L. Disorder in the pseudohexagonal rotator phase of *n*-alkanes: molecular-dynamics calculations for tricosane. *Mol. Phys.* **1989**, *67*, 957−979.
(24) Esselink, K.; Hilbers, P. A. J.; van Beest, B. W. H. Molecular dynamics study of nucleation and melting of *n*-alkanes. *J. Chem. Phys.* **1994**, *101*, 9033−9041.
(25) Tsuchiya, Y.; Hasegawa, H.; Iwatsubo, T. Prediction of the melting point of *n*-alkanes using the molecular dynamics method. *J. Chem. Phys.* **2001**, *114*, 2484−2488.
(26) Wentzel, N.; Milner, S. T. Crystal and rotator phases of n-alkanes: A molecular dynamics study. *J. Chem. Phys.* **2010**, *132*, DOI: .
(27) Burrows, S. A.; Korotkin, I.; Smoukov, S. K.; Boek, E.; Karabasov, S. Benchmarking of Molecular Dynamics Force Fields for Solid−Liquid and Solid−Solid Phase Transitions in Alkanes. *J. Phys. Chem. B* **2021**, *125*, 5145−5159.
(28) Wentzel, N.; Milner, S. T. Simulation of multiple ordered phases in C23 *n*-alkane. *J. Chem. Phys.* **2011**, *134*, DOI: .
(29) Burrows, S. A.; Lin, E. E.; Cholakova, D.; Richardson, S.; Smoukov, S. K. Structure of the Hexadecane Rotator Phase: Combination of X-ray Spectra and Molecular Dynamics Simulation. *J. Phys. Chem. B* **2023**, *127*, 7772−7784.
(30) Burrows, S. A.; Shon, J. W.; Peychev, B.; Slavchov, R. I.; Smoukov, S. K. Phase transitions of fluorotelomer alcohols at the water—alkane interface studied via molecular dynamics simulation. *Soft Matter* **2024**, *20*, 2243−2257.
(31) Lin, T.-S.; Coley, C. W.; Mochigase, H.; Beech, H. K.; Wang, W.; Wang, Z.; Woods, E.; Craig, S. L.; Johnson, J. A.; Kalow, J. A.; Jensen, K. F.; Olsen, B. D. BigSMILES: A Structurally-Based Line Notation for Describing Macromolecules. *ACS Central Science* **2019**, *5*, 1523−1531.
(32) Beromi, M. M.; Kennedy, C. R.; Younker, J. M.; Carpenter, A. E.; Mattler, S. J.; Throckmorton, J. A.; Chirik, P. J. Iron-catalysed synthesis and chemical recycling of telechelic 1,3-enchained oligocyclobutanes. *Nat. Chem.* **2021**, *13*, 156−162.
(33) Nie, C.; Maguire, S. M.; Zheng, C. W.; Mohadjer Beromi, M.; Register, R. A.; Priestley, R. D.; Davidson, E. C.; Chirik, P. J. A butadiene-derived semicrystalline polyolefin with two-tiered chemical recyclability. *Chem.* **2024**, *10*, 698−712.
(34) Black, D. R.; Mendenhall, M. H.; Brown, C. M.; Henins, A.; Filliben, J.; Cline, J. P. Certification of Standard Reference Material 660c for powder diffraction. *Powder Diffraction* **2020**, *35*, 17−22.
(35) Thompson, A. P.; Aktulga, H. M.; Berger, R.; Bolintineanu, D. S.; Brown, W. M.; Crozier, P. S.; in't Veld, P. J.; Kohlmeyer, A.; Moore, S. G.; Nguyen, T. D.; Shan, R.; Stevens, M. J.; Tranchida, J.; Trott, C.; Plimpton, S. J. LAMMPS - a flexible simulation tool for particle-based materials modeling at the atomic, meso, and continuum scales. *Comput. Phys. Commun.* **2022**, *271*, No. 108171.
(36) Hockney, R. W.; Eastwood, J. W.; *Computer Simulation Using Particles*; Adam Hilger, 1988; p 540.
(37) Hoover, W. G. Canonical dynamics: Equilibrium phase-space distributions. *Phys. Rev. A* **1985**, *31*, 1695−1697.
(38) Seo, B.; Lin, Z.-Y.; Zhao, Q.; Webb, M. A.; Savoie, B. M. Topology Automated Force-Field Interactions (TAFFI): A Framework for Developing Transferable Force Fields. *J. Chem. Inf. Model.* **2021**, *61*, 5013−5027.
(39) Williams, D. E. Nonbonded Potential Parameters Derived from Crystalline Hydrocarbons. *J. Chem. Phys.* **1967**, *47*, 4680−4684.
(40) Jorgensen, W. L.; Maxwell, D. S.; Tirado-Rives, J. Development and Testing of the OPLS All-Atom Force Field on Conformational Energetics and Properties of Organic Liquids. *J. Am. Chem. Soc.* **1996**, *118*, 11225−11236.
(41) Lin, Y.-S.; Li, G.-D.; Mao, S.-P.; Chai, J.-D. Long-Range Corrected Hybrid Density Functionals with Improved Dispersion Corrections. *J. Chem. Theory Comput.* **2013**, *9*, 263−272.
(42) Grimme, S.; Antony, J.; Ehrlich, S.; Krieg, H. A consistent and accurateab initioparametrization of density functional dispersion correction (DFT-D) for the 94 elements H-Pu. *J. Chem. Phys.* **2010**, *132*, DOI: .
(43) Schäfer, A.; Horn, H.; Ahlrichs, R. Fully optimized contracted Gaussian basis sets for atoms Li to Kr. *J. Chem. Phys.* **1992**, *97*, 2571−2577.
(44) Weigend, F.; Ahlrichs, R. Balanced basis sets of split valence, triple zeta valence and quadruple zeta valence quality for H to Rn: Design and assessment of accuracy. *Phys. Chem. Chem. Phys.* **2005**, *7*, 3297.
(45) Neese, F. The ORCA program system. *WIREs Computational Molecular Science* **2012**, *2*, 73−78.
(46) Breneman, C. M.; Wiberg, K. B. Determining atom-centered monopoles from molecular electrostatic potentials. The need for high sampling density in formamide conformational analysis. *J. Comput. Chem.* **1990**, *11*, 361−373.
(47) Coleman, S. P.; Spearot, D. E.; Capolungo, L. Virtual diffraction analysis of Ni [0 1 0] symmetric tilt grain boundaries. *Modell. Simul. Mater. Sci. Eng.* **2013**, *21*, No. 055020.
(48) Peng, L. M.; Ren, G.; Dudarev, S. L.; Whelan, M. J. Robust Parameterization of Elastic and Absorptive Electron Atomic Scattering Factors. *Acta Crystallographica Section A Foundations of Crystallography* **1996**, *52*, 257−276.
(49) Kraack, H. Homogeneous crystal nucleation in short polyethylenes. *Polymer* **2001**, *42*, 8225−8233.
(50) Deng, C.; Webb, M. A.; Bennington, P.; Sharon, D.; Nealey, P. F.; Patel, S. N.; de Pablo, J. J. Role of Molecular Architecture on Ion Transport in Ethylene oxide-Based Polymer Electrolytes. *Macromolecules* **2021**, *54*, 2266−2276.
(51) Peng, H.; Zhang, D.; Ling, X.; Li, Y.; Wang, Y.; Yu, Q.; She, X.; Li, Y.; Ding, Y. n-Alkanes Phase Change Materials and Their Microencapsulation for Thermal Energy Storage: A Critical Review. *Energy Fuels* **2018**, *32*, 7262−7293.
(52) Klein, J. P.; Register, R. A. Tuning the phase behavior of semicrystalline hydrogenated polynorbornene via epimerization. *J. Polym. Sci., Part B: Polym. Phys.* **2019**, *57*, 1188−1195.

https://doi.org/10.1021/acs.chemmater.4c02576
Chem. Mater. 2024, 36, 11596−11605